EFFECT OF STACKING 2D LEAD CHLORIDE PEROVSKITES INTO VERTICAL HETEROSTRUCTURES ON PHOTOLUMINESCENCE INTENSITY**

D. R. Graupner, D. S. Kilin*

Department of Chemistry and Biochemistry, North Dakota State University, Fargo, North Dakota, USA; e-mail: dmitri.kilin@ndsu.edu

Two-dimensional organic-inorganic hybrid lead halide perovskites are of interest for photovoltaic and light emitting devices due to their relative stability when compared to bulk lead halide perovskites and favorable properties that can be tuned. Tuning of the material can be performed by adjusting halide composition or by taking advantage of confinement effects. Here we use density functional theory and excited state dynamics treated by reduced density matrix method to examine the effects that varying the thickness of the perovskite layer has on the ground state and excited state photo-physical properties of the materials, further we explore the effects of a vertical heterostructure of perovskite layers. Nonadiabatic couplings were computed based on the on-the-fly approach along a molecular dynamic trajectory at ambient temperatures. Density matrix-based equation of motion for electronic degrees of freedom is used to calculate the dynamics of electronic degrees of freedom. We find that the vertical stacking of two-dimensional perovskites into heterostructures shows an increase in photoluminescence intensity by two orders of magnitude when compared to the individual two-dimensional perovskites.

Keywords: *photoluminescence, heterostructure, two-dimensional perovskites.*

ВЛИЯНИЕ УПАКОВКИ ДВУМЕРНЫХ ПЕРОВСКИТОВ НА ОСНОВЕ ХЛОРИДА СВИНЦА В ВЕРТИКАЛЬНЫЕ ГЕТЕРОСТРУКТУРЫ НА ИНТЕНСИВНОСТЬ ФОТОЛЮМИНЕСЦЕНЦИИ

D. R. Graupner, D. S. Kilin*

УДК 535.37:548.736.442.6

Университет штата Северная Дакота, Фарго, Северная Дакота, США; e-mail: dmitri.kilin@ndsu.edu

(Поступила 13 февраля 2023)

С использованием теории функционала плотности и динамики возбужденного состояния, обработанного методом приведенной матрицы плотности, изучено влияние изменения толщины слоя перовскита на фотофизические свойства 2D-перовскитов на основе галогенидов свинца в основном и возбужденном состояниях, далее исследованы эффекты вертикальной гетероструктуры слоев перовскита. Неадиабатические взаимодействия рассчитаны на основе подхода on-the-fly по траектории молекулярной динамики при температуре окружающей среды. Уравнение движения электронных степеней свободы на основе матрицы плотности используется для расчета динамики электронных степеней свободы. Обнаружено, что вертикальная укладка двумерных перовскитов в гетероструктуры приводит к увеличению интенсивности фотолюминесценции на два порядка по сравнению с отдельными двумерными перовскитами.

Ключевые слова: *фотолюминесценция, гетероструктура, двумерные перовскиты.*

Introduction. Full inorganic $CsPbX_3$ (X = Cl, Br, I) bulk lead halide perovskites (LHPs) have become popular candidates for next generation opto-electronic devices due to their high quantum yields, high color purity, tunable emission over the visible spectrum, and low cost [1, 2]. However, these materials show poor

** Полный текст публикуется в JAS V. 90, No. 2 (http://springer.com/journal/10812) и в электронной версии ЖПС Т. 90, № 2 (http://www.elibrary.ru/title_about.asp?id=7318; sales@elibrary.ru).

stability when exposed to moisture or photoirradiation [3—5]. This has led to the examination of two-dimensional inorganic-organic hybrid perovskites which offer increased stability [6] and higher tunability of physical properties [7, 8]. The first room-temperature perovskite light-emitting diodes (LEDs) were reported in 2014 [9] and have shown impressive progress with two-dimensional (2D) perovskite LEDs achieving 20.2% external quantum efficiency (EQE) in 2020 [10]. While there has been an increase in EQE for perovskite LEDs, there is still a need to generate high efficiency perovskite LEDs for pure colors to meet commercial viability [11, 12].

2D halide perovskites are defined by a stoichiometric formula $A'_{n'}A_{n-1}M_nX_{3n+1}$, A′ — monovalent or divalent cation; $n' = 2$ or 1; A = Cs^+, methylammonium (MA), formadamidinium (FA); M = Pb^{2+}, Sn^{2+}, etc.; X = Cl^-, Br^-, I^-), and are classified based on the thickness of the inorganic layer as indicated in the stochiometric formula (n = 1, 2, 3, etc.) and the stacking orientation of the inorganic layers ((100), (110), (111) with respect the ideal cubic perovskite) [13]. The layered structures of 2D perovskites can be divided into different categories; Dion–Jacobson (DJ) phase [14, 15], Ruddlesden–Popper (RP) phase [16], Aurivilius phase [17], and alternating cation in the interlayer space (ACI) [18]. The relative stacking of the layers results in the differences between these categories. The DJ perovskites show the ability to stack with no displacement due to the divalent interlayer spacers. 2D perovskites structures possess natural quantum-well structures, that induce both dielectric and quantum confinement effects [19]. The strong confinements lead to large exciton binding energies [20]. Further, it is observed that 2D perovskites often form in a mixed-phase structures rather than a single phase structures due to the similar formation energies of the different thickness 2D perovskites [21]. The mixed-phase 2D perovskites result in heterostructures that offer the possibilities of manipulation of the recombination, transport, and generation of charge carriers due to the change in band gap energies at the heterojunction [22].

Here we report the effects that combining 2D DJ LHPs into a vertical heterostructure provide for the photoluminescence (PL) of the materials. The combination of the different size layers is hoped to create an insulating effect that will increase the photoluminescence quantum yield (PLQY) of the thicker layer involved in the heterostructure. Examination of the ground state electronic properties of various 2D DJ LHPs by density functional theory (DFT) is performed to serve as a basis for the vertical heterostructure. To characterize the effect of the heterostructure on PL properties, we compute excited-state dissipative dynamics by computing the nonadiabatic couplings (NACs) between nuclear and electronic degrees of freedom from adiabatic molecular dynamics trajectories. Nonradiative relaxation rates are computed from the NACs using the reduced density matrix formalism within Redfield theory. PLQY is then computed from the nonradiative relaxation rates and radiative relaxation rates, computed from Einstein coefficients.

Methods. From the bulk $CsPbCl_3$ crystal structure, $2\times2\times n$ unit cells carved out, giving three Cs/Cl terminated surfaces and three Pb/Cl terminated surfaces providing a composition of $Cs_{4n}Pb_{4n}Cl_{12n}$. Four Cs atoms are removed from one face of the perovskite structure and replaced with butyl diammonium (BdA) molecules. Four Cl atoms are then added on the opposite end of the BdA molecules in line with the octahedral Pb/Cl structures from the initial crystal structure. Overall, this gives a structure of $BdA_4Cs_{4(n-1)}Pb_{4n}Br_{12n+4}$. The model has a simulation cell size of $10\times10\times(6+5.5n)$ Å^3 (Fig. 1).

DFT with the generalized gradient approximation (GGA) Perdew–Burke–Ernzerhof (PBE) functional [23] in a plane-wave basis set along with projector augmented-wave (PAW) pseudopotentials [24, 25] in Vienna ab initio Simulation Package (VASP) [26] software was used to calculate the ground-state electronic structure of our atomistic model. Subsequent single point calculations were performed using noncollinear spin DFT including the spin-orbit coupling (SOC) interaction and used to compute observables for the systems. All calculations were performed at the Γ point. The model is periodic.

Noncollinear spin DFT [27, 28] is used as the electronic basis, and we include the SOC interaction due to the large angular momentum of conduction band Pb^{2+} 6p orbitals. A self-consistent noncollinear spin DFT uses four densities $\rho_{\sigma\sigma'}(\mathbf{r})$ and rests on the Kohn-Sham (KS) equation:

$$\sum_{i,\sigma'=\alpha,\beta}\left(-\delta_{\sigma\sigma'}\nabla^2+v^{\text{eff}}_{\sigma\sigma'}\left[\rho_{\sigma\sigma'}(\mathbf{r})\right]\right)\varphi_{i\sigma}(\mathbf{r})=\varepsilon_i\ \varphi_{i\sigma'}(\mathbf{r}), \quad (1)$$

where $v^{\text{eff}}_{\sigma\sigma'}\left[\rho_{\sigma\sigma'}(\mathbf{r})\right]$ is the 2×2 matrix operator of effective potential and α and β are orthogonal spin indices. In accordance with the self-consistent theorem KS, the 2×2 effective potential is a functional of the electron-

ic density for a N electron system $v_{\sigma\sigma'}^{\text{eff}} = \dfrac{\delta E^{\text{tot}}\left[\rho_{\sigma\sigma'}^{N}\right]}{\delta\rho_{\sigma\sigma'}^{N}}$. Solutions of Eq. (1) produce spinor KS orbitals (SKSOs), which are two component wavefunctions composed of a superposition of $|\alpha\rangle$ and $|\beta\rangle$ spin components:

$$\varphi_i^{\text{SKSO}}(\mathbf{r}) = \begin{Bmatrix} \varphi_{i\alpha}(\mathbf{r}) \\ \varphi_{i\beta}(\mathbf{r}) \end{Bmatrix} = \varphi_{i\alpha}(\mathbf{r})\left|\alpha\right\rangle + \varphi_{i\beta}(\mathbf{r})\left|\beta\right\rangle . \tag{2}$$

Within the noncollinear spin DFT framework, relativistic effects can be incorporated using second-order scalar relativistic corrections:

$$H^{\text{rel}} = H^{\text{SR}} + H^{\text{SOC}} , \tag{3}$$

where H^{SR} the scalar relativistic term and H^{SOC} is the SOC term. The H^{SR} term describes relativistic kinetic energy corrections and H^{SOC} describes energy shifts of spin occupations. Up to the second order, H^{SOC} is represented as

$$H^{\text{SOC}} = \frac{\hbar}{4m^2c^2}\frac{1}{r}\frac{\partial v_{\text{sphere}}^{\text{KS}}}{\partial r}\mathbf{L}\cdot\mathbf{S} , \tag{4}$$

where **L** is the angular momentum operator and **S** is composed of Pauli spin matrices.

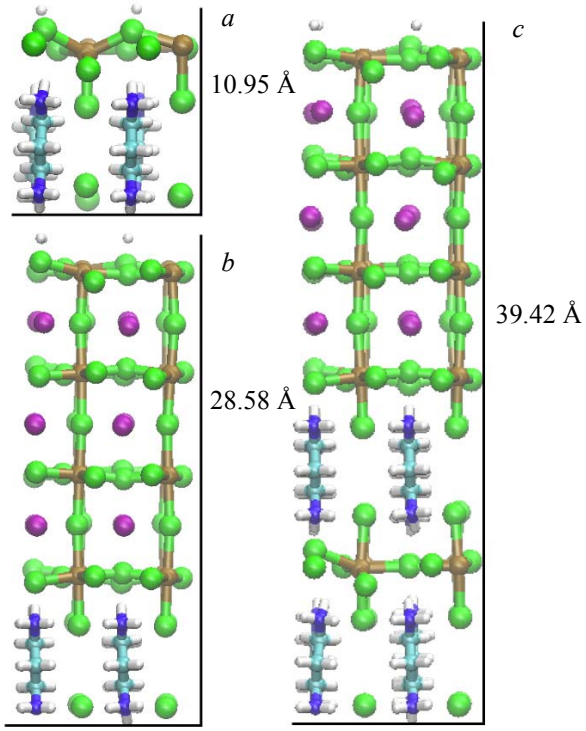

Fig. 1. Atomistic models of lead chloride organic-inorganic hybrid perovskite. Two models contain a single layer of perovskite where thickness of the perovskite layer is (a) n = 1 and (b) n = 4. The third model is a (c) vertical heterostructure that contains both a n = 1 and n = 4 perovskite layer. White, cyan, blue, brown, green, and purple spheres represent hydrogen, carbon, nitrogen, lead, chlorine, and cesium atoms, respectively.

For each model, we computed the electronic density of states DOS:

$$\text{DOS}_{\text{SKSO}} = \sum_i \delta\left(\varepsilon - \varepsilon_i^{\text{SKSO}} - \varepsilon_{\text{F}}\right), \tag{5}$$

where $\varepsilon_i^{\text{SKSO}}$ is the band eigenenergy and ε_{F} is the Fermi level $\varepsilon_{\text{F}} = \left(\varepsilon_i^{\text{SKSO},HOMO} + \varepsilon_i^{\text{SKSO},LUMO}\right)/2$. We use the independent orbital approximation (IOA) in which excited states are described as a pair of orbitals, as opposed to a superposition of orbitals commonly used in TDDFT or Bethe–Saltpeter approaches. Optical

transitions between SKSO *i* and *j* can be found through transition dipole matrix elements, which can be used to compute oscillator strengths:

$$\left\langle \mathbf{D}_{ij} \right\rangle = e\int d\mathbf{r}\left\{\varphi_{i\alpha}^{*} \quad \varphi_{i\beta}^{*}\right\}\mathbf{r}\begin{Bmatrix}\varphi_{j\alpha}\\ \varphi_{j\beta}\end{Bmatrix}, \tag{6}$$

$$f_{ij} = \left|\mathbf{D}_{ij}\right|^2 \frac{4\pi m_e \nu_{ij}}{3\hbar e^2}, \tag{7}$$

where ν_{ij} represents the transition frequency between SKSO *i* and *j*. The transition frequency ν_{ij} is related to the transition energy ΔE_{ij} by $h\nu_{ij} = \Delta E_{ij}$. With known oscillator strengths, an absorption spectrum can be computed through:

$$\alpha^{\mathrm{SKSO}}(\varepsilon) = \sum_{i<j} f_{ij}\delta\left(\hbar\omega - \hbar\omega_{ij}\right)\left\{\rho_{ii}^{\mathrm{eq}} - \rho_{jj}^{\mathrm{eq}}\right\}. \tag{8}$$

To dynamically couple electronic and nuclear degrees of freedom, we used adiabatic molecular dynamics (MD). This provides kinetic energy of nuclei to break orthogonality of electronic states. The nuclear degrees of freedom are treated in the classical path approximation (CPA) with the nuclei following the classical path trajectories. The initial velocities of nuclei are scaled to keep a constant temperature with forces acting on the nuclei depending on the:

$$\sum_{I=1}^{N^{\mathrm{ion}}} \frac{M_I}{2}\left(\frac{d\mathbf{R}_I}{dt}\Big|_{t=0}\right)^2 = \frac{3}{2}N^{\mathrm{ion}}k_B T, \tag{9}$$

$$\frac{d^2}{dt^2}\mathbf{R}_I = \mathbf{F}_I\left(\hat{\rho}_{\sigma\sigma'}^{N}\right)/M_I, \tag{10}$$

where $\mathbf{R}_I$ represents ionic coordinates; M_I mass of the I^{th} nuclei; k_B is the Boltzmann constant; T is temperature; and $\mathbf{F}_I\left(\left[\hat{\rho}\right]\right)$ is the force acting on the ions which we specify is a functional of the electronic density.

The Redfield quantum master equation [29, 30] in the density matrix formalism is used to describe the time evolution of electronic degrees of freedom that are weakly coupled to a thermal bath. Typical implementation of Redfield approach assumes the Markov approximation, where the model is immersed into a heat bath so that the bath temperature is constant as the bath is infinitely larger than the model of explicit interest.

$$\frac{d}{dt}\hat{\rho} = -\frac{i}{\hbar}\sum_k\left(F_{ik}\rho_{kj} - \rho_{ik}F_{kj}\right) + \left(\frac{d\rho_{ij}}{dt}\right)_{\mathrm{diss}}, \tag{11}$$

where F is the many-electron Fock matrix, which includes exchange and correlation, and ρ is the density matrix. The first term is the Liouville von Neumann equation describing the unitary time evolution of a closed system, while the second term describes electronic energy dissipation due to weak coupling to a thermal bath. The dissipative transitions are parameterized from NACs computed 'on-the-fly' in the basis of SKSO orbitals

$$\hat{V}_{ij}^{\mathrm{NA}}(t) = -i\hbar\left\langle \varphi_i^{\mathrm{SKSO}}\left(\mathbf{r},\left\{\mathbf{R}_I(t)\right\}\right)\left|\frac{\partial}{\partial t}\right|\varphi_j^{\mathrm{SKSO}}\left(\mathbf{r},\left\{\mathbf{R}_I(t)\right\}\right)\right\rangle =$$

$$= -\frac{i\hbar}{2\Delta t}\int d\mathbf{r}\left\{\varphi_{i\alpha}^{*}\left(\mathbf{r},\left\{\mathbf{R}_I(t)\right\}\right),\ \varphi_{i\beta}^{*}\left(\mathbf{r},\left\{\mathbf{R}_I(t)\right\}\right)\right\}\begin{Bmatrix}\varphi_{i\alpha}\left(\mathbf{r},\left\{\mathbf{R}_I(t+\Delta t)\right\}\right)\\ \varphi_{i\beta}\left(\mathbf{r},\left\{\mathbf{R}_I(t+\Delta t)\right\}\right)\end{Bmatrix} + \mathrm{h.c.} \tag{12}$$

Due to the nuclear kinetic energy of nuclei, the orthogonality relation is broken and provides a 'mixing' of SKSOs. NACs are converted into rates of transitions by taking the Fourier transform of the autocorrelation function

$$M_{ijkl}(\tau) = \frac{1}{T}\int_0^T V_{ij}^{\mathrm{NA}}\left(t+\tau\right)V_{kl}^{\mathrm{NA}}(t)t,$$

$$\Gamma_{ijkl}^{+} = \frac{1}{T}\int_0^T M_{ijkl}\left(\tau\right)e^{-i\omega_{ij}\tau}d\tau, \tag{13}$$

$$\Gamma_{ijkl}^{-} = \frac{1}{T}\int_0^T M_{ijkl}(\tau)e^{-i\omega_{kl}\tau}d\tau,$$

which provides components for the Redfield tensor:

$$R_{ijkl} = \Gamma^{+}_{ljik} + \Gamma^{-}_{kijl} - \delta_{jl}\sum_m \Gamma^{+}_{immk} - \delta_{ik}\sum_m \Gamma^{-}_{jmml} . \quad (14)$$

The Redfield tensor controls the dissipative dynamics of the density matrix:

$$\left(\frac{d\rho_{ij}}{dt}\right)_{\text{diss}} = \sum_{lm} R_{ijlm}\rho_{lm} . \quad (15)$$

From the Redfield tensor R_{ijkl} we can approximate a nonradiative recombination rate k_{nr} from Redfield matrix elements

$$k_{\text{nr}} \approx R_{HO-LU} . \quad (16)$$

Along the excited-state trajectory we can compute time-resolved observables such as changes in charge carrier occupations:

$$n^{(a,b)}(\varepsilon,t) = \sum_i \rho_{ii}^{(a,b)}(t)\delta\left(\varepsilon - \varepsilon_i\right), \ \Delta n^{(a,b)}(\varepsilon,t) = n^{(a,b)}(\varepsilon,t) - n^{eq}(\varepsilon,t) , \quad (17)$$

and average charge carrier energy

$$\left\langle \Delta\varepsilon_e(t)\right\rangle = \sum_{i\geq LU}\rho_{ii}(t)\varepsilon_i(t) , \ \left\langle \Delta\varepsilon_h(t)\right\rangle = \sum_{i\leq HO}\rho_{ii}(t)\varepsilon_i(t) . \quad (18)$$

To get the rates of charge carrier relaxation to band edges, we convert the energy expectation value from Eq. (18) into dimensionless energy Eq. (19). We fit Eq. (19) to an exponential decay, assuming a single exponential decay, and solve for the rate constant k_e Eq. (20).

$$\left\langle E_{e/h}\right\rangle(t) = \frac{\left\langle \Delta E_{e/h}\right\rangle(t) - \left\langle \Delta E_{e/h}\right\rangle(\infty)}{\left\langle \Delta E_{e/h}\right\rangle(0) - \left\langle \Delta E_{e/h}\right\rangle(\infty)} , \quad (19)$$

$$k_{e/h} = \left\{\tau_{e/h}\right\}^{-1} = \left\{\int_0^\infty E_{e/h}(t)dt\right\}^{-1} . \quad (20)$$

Time-resolved emission in the excited state can be found based on the presence of inverse occupations along the excited-state trajectory and the intensity of oscillator strength between states i and j:

$$E\left(\hbar\omega,t\right) = \sum_{j>i} f_{ij}\delta\left(\hbar\omega - \hbar\omega_{ij}\right)\left\{\rho_{jj}(t) - \rho_{ii}(t)\right\} . \quad (21)$$

An emission spectrum can be generated by integrating the time-resolved emission along the trajectory:

$$E^{\text{tot}}\left(\hbar\omega\right) = \frac{1}{T}\int_0^T E\left(\hbar\omega,t\right)dt . \quad (22)$$

Rates of radiative recombination k_{r} can be found from Einstein coefficients for spontaneous emission [31]:

$$k_{\text{r}} = A_{HO\text{-}LU} = \frac{8\pi^2\nu_{HO\text{-}LU}^2 e^2}{\varepsilon_0 m_e c^3}\frac{g_i}{g_j} / f_{HO\text{-}LU} , \quad (23)$$

where $f_{HO–LU}$ is the oscillator strength, $\nu_{HO\text{-}LU}$ represents the transition frequency for the $HO–LU$ transition where $i = HO$ and $j = LU$, g_i is the degeneracy of the ith electronic state, and the rest of the variables represent the fundamental constants. From the radiative recombination rate k_r and k_{nr} we compute a PLQY:

$$\text{PLQY} = \frac{k_{\text{r}}}{k_{\text{r}} + k_{\text{nr}}} . \quad (24)$$

Results and discussion. In Figs. 2a,b we examine the ground state density of states (DOS) for the three models studied here. Peaks are labeled with numbers (prime numbers) that increase as they move away from the bandgap. The electronic structure of the $n = 1$ and $n = 4$ single layer models serve as a basis for the examination of the electronic structure of the heterostructure model for properties inherent to the single layer models. It is observed that the heterostructure model shows a similar pattern of peaks compared to the $n = 4$ single layer model only approximately 0.2 eV higher in energy. Due to the use of noncollinear spin approach with spin-orbit coupling we see a narrowing of the bandgap. Figure 2c shows the projected density of states (PDOS) for the heterostructure model. We note that the first band in both the conduction and valence band is localized entirely on the $n = 4$ layer of the model, which we attribute to the $n = 4$ region showing less quantum-confinement resulting in lower energy. It is not until the first sub-band that we see a contribution from the $n = 1$ layer of the model. The organic layer is seen to provide minimal contribution to the electronic structure over the region that we have studied. Computed absorption spectra, shown in Fig. 2d, are labeled with the transitions that contribute to the peaks based on the numerical labeling of the pair of peaks in the DOS. It is observed that the transitions that contribute to the peak pattern for both the $n = 4$ single layer and

the heterostructure are the same with the energy for the transitions in the heterostructure model being about 0.4 eV greater than the corresponding transition in the $n = 4$ single layer model.

NACs between SKSOs i and j computed using Eq. (12), are used to determine nonradiative relaxation dynamics of the photoexcited states. The Redfield tensors, R_{ijij} depend on the NACs and are illustrated in Fig. 3 for the $n = 1$ single layer, $n = 4$ single layer, and heterostructure models. The Redfield tensors represent the rates of state-to-state transitions in units of ps^{-1}. These rates are used to compute nonradiative recombination rates k_{nr} Eq. (16). Note that only off diagonal tensor elements are nonzero while all diagonal elements are zero. For Fig. 3a–c it is observed that there are alternating high intensity transitions near the main diagonal and numerous low intensity transitions away from the main diagonal. The R_{ijij} value for the *HO–LU* transition is of particular interest due to its use for calculating the PLQY of the models. The alternating high intensity transitions are between near-degenerate states, which result from the inclusion of spin-orbit coupling into the calculations.

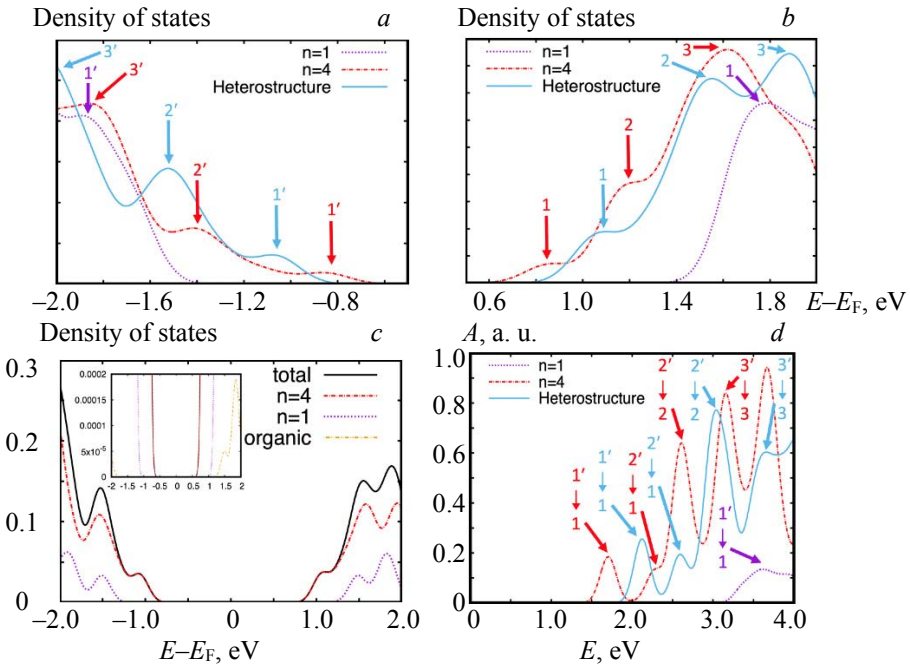

Fig. 2. (a) Conduction band and (b) valence band density of states for ground state $n = 1$ single layer, $n = 4$ single layer, and heterostructure models. Arrows are used as labels for the peaks in the band structure. Valence band peaks are labeled using natural numbers, larger numbers are deeper in the valence band. Conduction band peaks are labeled by prime-natural numbers, larger numbers are deeper in the valence band. (c) Projected density of states for the heterostructure model. Inset shows a closer view of the PDOS. (d) Computed absorption spectra, Eq. (8), for $n = 1$ single layer, $n = 4$ single layer, and heterostructure models. Arrows show the transition for the absorption contributed by transitions from a pair of peaks A→A′ in valence and conduction band.

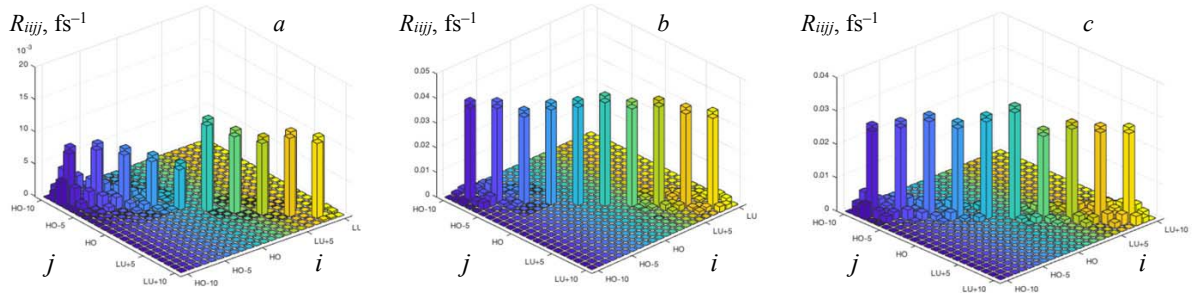

Fig. 3. Redfield tensor for (a) $n = 1$ single layer, (b) $n = 4$ single layer, and (c) heterostructure models. The R_{ijij} axis represents the nonradiative state to state transition rates. The alternating high intensity transitions near the main diagonal are between near-degenerate states; i and j are orbital indexes.

Figure 4 show hot-carrier cooling along the excited-state trajectory for $n = 1$ single layer, $n = 4$ single layer, and heterostructure models from a nonequilibrium state to the first excited state. The initial conditions for the $n = 1$ and $n = 4$ single layer models represent the highest oscillator strength excitation that does not involve one of the near-degenerate principal band gap orbitals. The initial condition for the heterostructure model represents the highest oscillator strength transition that occurs on the $n = 1$ layer in the model. The energy axis is in reference to the Fermi level of the model with the time axis in log scale normalized to 1 ps. The green color indicates background reference charge density, blue indicates the average occupation of charge density distribution in the valence band, and yellow indicates the average occupation of charge density distribution in the conduction band. Horizontal dotted/solid lines represent the energy expectation values of charge carriers Eq. (19). The vertical dashed lines labeled with τ_h and τ_e Eq. (20), represent time of relaxation from *HO–x* to *HO* and *LU+y* to *LU*, respectively. For the single layer models, it is observed that there is a long lived, compared to the $k_{e/h}$, population in a higher excited state than the first excited state. This is attributed to a mismatch between electronic transition energy and available normal modes.

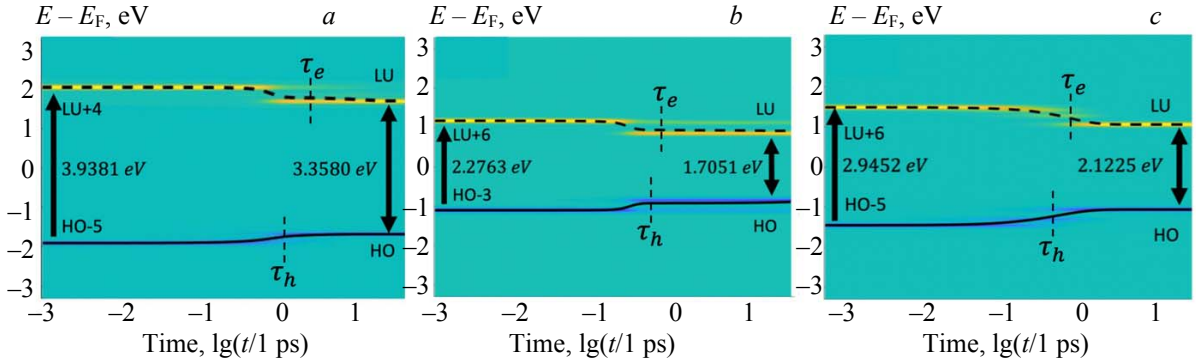

Fig. 4. Nonradiative relaxation for the (a) $n = 1$ single layer, (b) $n = 4$ single layer, and (c) heterostructure models. The yellow line represents the charge density of the electron, while the blue line represents the charge density of the hole. The vertical dashed lines labeled with τ_h and τ_e represent time of relaxation from *HO–x* and *LU+y*, respectively. The horizontal solid and dashed lines show the energy expectation value for the hole and electron, respectively. The initial conditions for the $n = 1$ and $n = 4$ single layer models represent the highest oscillator strength excitation that does not involve one of the near-degenerate principal band gap orbitals. The initial condition for the heterostructure model represents the highest oscillator strength transition that occurs on the $n = 1$ layer in the model. All cases show both the blue and yellow line starting at a greater distance from each other and moving closer to each other. τ_h and τ_e or the single layer models occur after the energy expectation values approach the band gap energies due to relatively long-lived excited states.

A competing mechanism for nonradiative dissipation is radiative relaxation in the form of photons. Figures 5a,b show the time-resolved (Eq. (21)) and time-integrated (Eq. (22)) emission for the $n = 1$ single layer model along the excited state trajectory. Figures 5c–f show the same plots for the $n = 4$ single layer and heterostructure models, respectively. The blue background color corresponds to no photoluminescence (PL) at a given time and transition energy, while the natural colors from blue to yellow correspond to the intensity of the PL. It is observed that there is an initial emission event at the initial excitation before cooling to the bandgap. Once the hot-carriers cool to the bandgap we see emission arising from the *HO–LU* transitions. Figures 5b,d,f show the time-integrated intensity for the transitions along the trajectory. The $n = 4$ model shows a higher relative intensity of the intra-band emissions when compared the *HO–LU* transition, which is attributed to the long-lived excited state for this model. It is seen that the emission at the *HO–LU* transition is the most intense transition for all the models. However, we observe that the intensity of the *HO–LU* transition for the heterostructure model is 2 orders of magnitude greater than the *HO–LU* transition for the $n = 1$ single layer model and 3 orders of magnitude greater than for the $n = 4$ single layer model.

To determine the efficiency of PL for the single layer and heterostructure models, we compute PLQY (Eq. (24)) from k_r and k_{nr}. The Einstein coefficient for spontaneous emission in terms of oscillator strength is used to calculate k_r (Eq. (23)) and the corresponding Redfield tensor element $R_{HO\text{-}LU}$ is used for k_{nr} (Eq. (16)). Table 1 shows the k_r, k_{nr}, and PLQY for the models presented here. The PLQY noted in the

Table 1 is calculated as an average value of the PLQY calculated for all the *HO–LU* degenerate transitions. It is observed that the heterostructure models shows a higher PLQY than the single layer models.

TABLE 1. Oscillator Strength f_{ij} (Eq. (7), Radiative Recombination Rate k_r (Eq. (23)), Nonradiative Recombination rate k_{nr} (Eq. (16)), Resultant PLQYs for Each Model Studied (Eq. (24))

Model	f_{ij}	k_r,1/fs	k_{nr},1/fs	PLQY
n = 1 single layer	0.32	2.00×10^{-6}	1.86×10^{-6}	0.3326
n = 4 single layer	0.07	2.64×10^{-6}	2.81×10^{-6}	0.3355
Heterostructure	0.60	3.22×10^{-6}	1.21×10^{-6}	0.6667

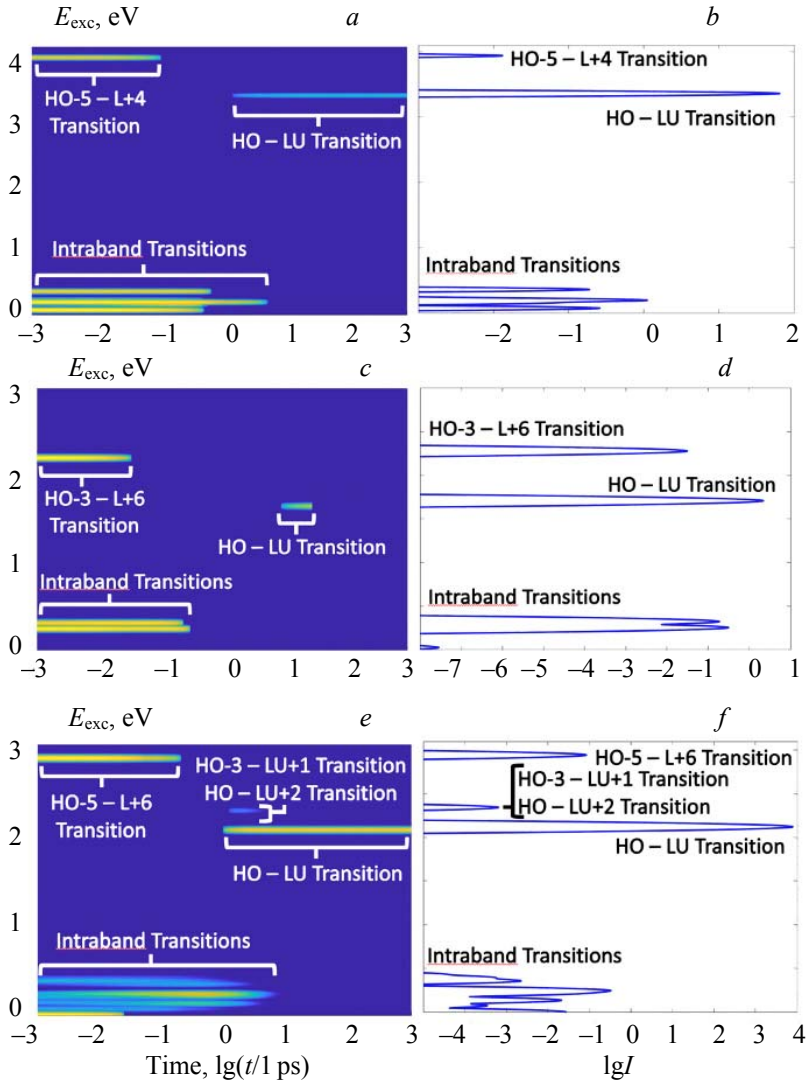

Figure 5. Radiative relaxation along the excited-state electronic dynamics trajectory with (a, c, e) showing time-resolved emission and (b, d, f) showing time-integrated radiative emission for the (a, b) n = 1 single layer, (c, d) n=4 single layer, and (e, f) heterostructure models. The initial conditions for this figu-re correspond to those in Fig. 4. The blue background corresponds to no PL at a given time and transition energy. Natural colors from blue to yellow correspond to intensity of the time-resolved PL. For each model, it is observed that the *HO–LU* transition is the most intense. We observed that the *HO–LU* transition for the heterostructure shows two orders of magnitude greater intensity than the n = 1 single layer and three order of magnitude greater intensity than the n = 4 single layer.

Lifetimes characterizing charge carrier dissipative electronic dynamics trajectories for the hole and electron; τ_h and τ_e (Eq. (20)) represent time of relaxation from *HO–x* to *HO* and *LU+y* to *LU*, respectively (Fig. 6). It is observed that for the hole and the electron in the heterostructure we see a linear relationship between dissipation energy and charge carrier lifetime. This linear relationship is in agreement with the energy gap law; however, this relationship only holds true for dissipation energy above 0.5 eV for the $n = 4$ single layer model and 1.0 eV for the $n = 1$ single layer model.

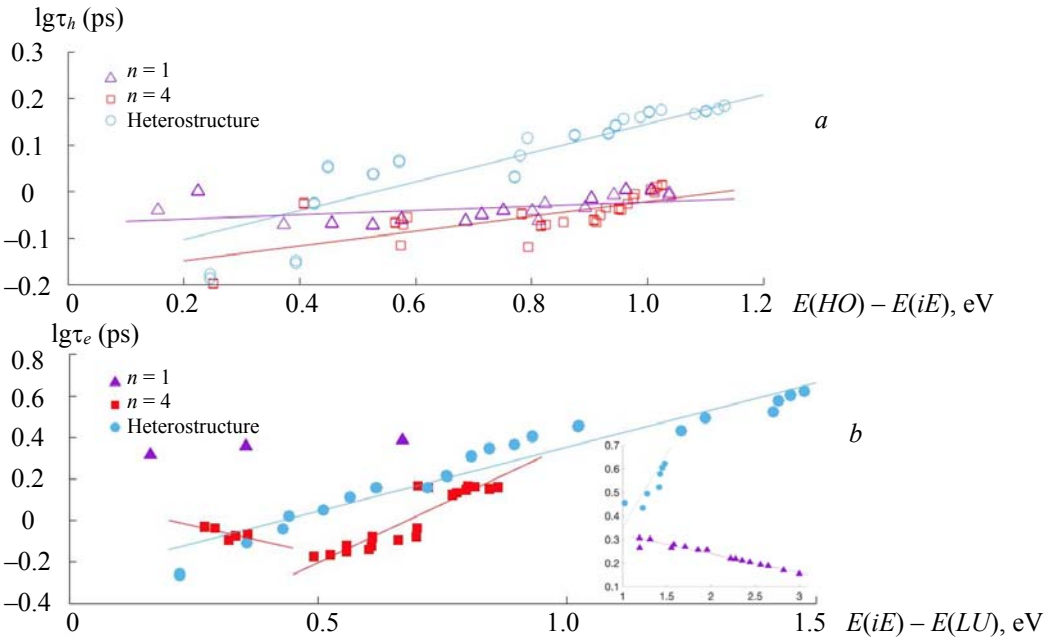

Fig. 6. Lifetimes characterizing charge carrier dissipative electronic dynamics trajectories for the (a) hole and (b) electron, inset shows high dissipation energy region for the electron. It is observed that for the hole and the electron in the heterostructure we see a linear relationship between dissipation energy and charge carrier lifetime. This linear relationship is in agreement with the energy gap law. This relationship only holds true for dissipation energy above 0.5 eV for the $n = 4$ single layer model and 1.0 eV for the $n = 1$ single layer model.

The intensities of the emission at the *HO–LU* transitions are greater than the intensities for any other transition for their respective model due to the increased lifetime of emission for the *HO–LU* transition. The increased intensity of the *HO–LU* transition for the heterostructure model compared to the single layer models is attributed to the increased relative size of the spacer region of the structure. In the $n = 4$ single layer model the perovskite layers are separated by a single butyl diammonium space. Although this organic carbon chain is an insulator, its short length may allow some level of hybridization between separate $n = 4$ layers. In the heterostructure model, each $n = 4$ layer of perovskite is separated by two butyl diammonium spacers and a $n = 1$ perovskite layer, all of a higher gap than the $n = 4$ perovskite layer. This is more than double the separation between the $n = 4$ perovskite layers making them more isolated. This isolation prevents hybridization of the electron and hole beyond the border of the slab and hypothetically confines the electron and hole in the same spatial region. This activity of the spacers is expected to increase the transition dipole, and by extension the oscillator strength. This is analogous to the passivation of semiconductor nanocrystals with organic ligands of extended length.

The intensity of the emission for the *HO–5–LU+6* transition for the heterostructure model shows the second highest intensity for this structure and has an energy comparable to the *HO–LU* transition energy for the $n = 1$ single layer model. This indicates the potential for dual emission with energies that correspond to both the $n = 1$ and $n = 4$ single layer models. This would be an indication that these models may not follow Kasha's rule [32]. This duel emission is in agreement to the multiple emission found experimentally [33].

Table 1 shows the oscillator strength, non-radiative and radiative rates of relaxation, and photoluminescence quantum yield for the three models of interest. The oscillator strength shown here is for the *HO–LU*

transition but the radiative and nonradiative rates of relaxation and PLQY shown factor in all four transitions between the near-degenerate *HO–LU* states. Due to this, we see a larger radiative recombination rate and PLQY for the $n = 4$ single layer model than would be expected looking just at the oscillator strength reported in Table 1. The combination of the near-degenerate transitions also affects the relative difference in PLQY of the models when compared to their PL intensity. The larger PLQY for the heterostructure is due to the consistent nature of the radiative recombination rate across these four transitions, in addition to have a smaller nonradiative recombination rate, compared to the single layer models. The single layer models by comparison show two transitions where the radiative rate of relaxation is an order of magnitude lower than for the heterostructure model.

Conclusions. Here we use density functional theory and nonadiabatic excited-state dynamics calculations to explore the photo-physical properties of single layer and vertical heterostructures of two-dimensional hybrid lead chloride perovskites. We observed an increase in intensity of the photoluminescence for the vertical heterostructure 2D lead halide perovskites attributed to the increase in effective insulation between the perovskite layers. Radiative dynamics show that for the single layer models there is a smaller relative intensity of emission when compared to the vertical heterostructure model. The smaller intensity in the single layer models is attributed to the smaller relative size of the space between layers allowing for a greater overlap of orbitals/bands/ between layers. In the heterostructure model, this space between the larger $n = 4$ perovskite layers in adjacent periodic cells is made up of two organic layers and a smaller $n = 1$ layer of perovskite, all of which have a larger gap than the $n = 4$ perovskite layers. This increased separation prevents the overlap across multiple layers and confines the electron and hole in the same spatial region.

It is also seen for the heterostructure model that there is a radiative emission around the same energy as the $n = 1$ single layer model, though lower in intensity than the *HO–LU* transition emission. This indicates that it may be possible to observe effects from the individual layers of the heterostructure model separately and that these models may not follow Kasha's rule.

This has the potential to lead to an improvement in the efficiency of perovskite light emitting diodes. However, two important areas for continued research are the evaluation of polarons in the perovskites and the inclusion of momentum dispersion in the calculations.

Acknowledgements. D.G. Thanks NSF CHE-2004197 for support. D.K. acknowledges the support of the National Science Foundation under Grant CHE-1944921. Authors thank the DOE BES NERSC facility for computational resources, allocation award "Computational Modeling of Photo-catalysis and Photo-induced Charge Transfer Dynamics on Surfaces", supported by the Office of Science of the DOE under Contract DE-AC02-05CH11231. Authors also thank Aaron Forde, Yulun Han, Landon Johnson, Steven Westra, and Amirhadi Alesadi for collective discussion and editing. D.K. thanks David Micha, Oleg Prezhdo, Sergei Tretiak, Svetlana Kilina, Andrei Kryjevski for inspiring discussions.

REFERENCES

1. L. Protesescu, S. Yakunin, M. I. Bodnarchuk, F. Krieg, R. Caputo, C. H. Hendon, R. X. Yang, A. Walsh, M. V. Kovalenko, *Nano Lett.*, **15**, No. 6, 3692 (2015), doi: 10.1021/nl5048779.
2. B. R. Sutherland, E. H. Sargent, *Nat. Photonics*, **10**, No. 5, 295 (2016), doi: 10.1038/nphoton.2016.62.
3. X. Chen, H. Zhou, H. Wang, *Front. Chem.*, **9** (2021), doi: 10.3389/fchem.2021.715157.
4. E.-B. Kim, M. S. Akhtar, H.-S. Shin, S. Ameen, M. K. Nazeeruddin, *J. Photochem. Photobiol.*, *C* **48**, 100405 (2021), doi: 10.1016/j.jphotochemrev.2021.100405.
5. C. Ma, C. Leng, Y. Ji, X. Wei, K. Sun, L. Tang, J. Yang, W. Luo, C. Li, Y. Deng, S. Feng, J. Shen, S. Lu, C. Du, H. Shi, *Nanoscale*, **8**, No. 43, 18309 (2016), doi: 10.1039/C6NR04741F.
6. F. Arabpour Roghabadi, M. Alidaei, S. M. Mousavi, T. Ashjari, A. S. Tehrani, V. Ahmadi, S. M. Sadrameli, *J. Mater. Chem. A*, **7**, No. 11, 5898 (2019), doi:10.1039/C8TA10444A.
7. G. E. Eperon, S. D. Stranks, C. Menelaou, M. B. Johnston, L. M. Herz, H. J. Snaith, *Energy Environ. Sci.*, **7**, No. 3, 982 (2014), doi:10.1039/C3EE43822H.
8. T. M. Koh, V. Shanmugam, J. Schlipf, L. Oesinghaus, P. Muller-Buschbaum, N. Ramakrishnan, V. Swamy, N. Mathews, P. P. Boix, S. G. Mhaisalkar, *Adv. Mater.*, **28**, No. 19, 3653 (2016), doi: 10.1002/adma.201506141.
9. Z.-K. Tan, R. S. Moghaddam, M. L. Lai, P. Docampo, R. Higler, F. Deschler, M. Price, A. Sadhanala, L. M. Pazos, D. Credgington, F. Hanusch, T. Bein, H. J. Snaith, R. H. Friend, *Nat. Nanotechnol.*, **9**, No. 9, 687 (2014), doi: 10.1038/nnano.2014.149.

10. Y. Miao, L. Cheng, W. Zou, L. Gu, J. Zhang, Q. Guo, Q. Peng, M. Xu, Y. He, S. Zhang, Y. Cao, R. Li, N. Wang, W. Huang, J. Wang, *Light: Sci. Appl.*, **9**, No. 1, 89 (2020), doi: 10.1038/s41377-020-0328-6.
11. L. Zhang, C. Sun, T. He, Y. Jiang, J. Wei, Y. Huang, M. Yuan, *Light: Sci. Appl.*, **10**, No. 1, 61 (2021), doi: 10.1038/s41377-021-00501-0.
12. C. Zhao, D. Zhang, C. Qin, *CCS Chem.*, **2**, No. 4, 859 (2020), doi: 10.31635/ccschem.020.202000216.
13. L. Mao, W. Ke, L. Pedesseau, Y. Wu, C. Katan, J. Even, M. R. Wasielewski, C. C. Stoumpos, M. G. Kanatzidis, *J. Am. Chem. Soc.*, **140**, No. 10, 3775 (2018), doi: 10.1021/jacs.8b00542.
14. M. Dion, M. Ganne, M. Tournoux, *Mater. Res. Bull.*, **16**, No. 11, 1429 (1981), doi: 10.1016/0025-5408(81)90063-5.
15. A. J. Jacobson, J. W. Johnson, J. T. Lewandowski, *Inorg. Chem.*, **24**, No. 23, 3727 (1985), doi: 10.1021/ic00217a006.
16. C. C. Stoumpos, D. H. Cao, D. J. Clark, J. Young, J. M. Rondinelli, J. I. Jang, J. T. Hupp, M. G. Kanatzidis, *Chem. Mater.*, **28**, No. 8, 2852 (2016), doi: 10.1021/acs.chemmater.6b00847.
17. K. R. Kendall, C. Navas, J. K. Thomas, H.-C. zur Loye, *Chem. Mater.*, **8**, No. 3, 642 (1996), doi: 10.1021/cm9503083.
18. C. M. M. Soe, C. C. Stoumpos, M. Kepenekian, B. Traoré, H. Tsai, W. Nie, B. Wang, C. Katan, R. Seshadri, A. D. Mohite, J. Even, T. J. Marks, M. G. Kanatzidis, *J. Am. Chem. Soc.*, **139**, No. 45, 16297 (2017), doi: 10.1021/jacs.7b09096.
19. K. Wang, J. Y. Park, Akriti, L. Dou, *EcoMat*, **3**, No. 3, e12104 (2021), doi: 10.1002/eom2.12104.
20. J. C. Blancon, A. V. Stier, H. Tsai, W. Nie, C. C. Stoumpos, B. Traoré, L. Pedesseau, M. Kepenekian, F. Katsutani, G. T. Noe, J. Kono, S. Tretiak, S. A. Crooker, C. Katan, M. G. Kanatzidis, J. J. Crochet, J. Even, A. D. Mohite, *Nat. Commun.*, **9**, No. 1, 2254 (2018), doi: 10.1038/s41467-018-04659-x.
21. L. N. Quan, M. Yuan, R. Comin, O. Voznyy, E. M. Beauregard, S. Hoogland, A. Buin, A. R. Kirmani, K. Zhao, A. Amassian, D. H. Kim, E. H. Sargent, *J. Am. Chem. Soc.*, **138**, No. 8, 2649 (2016), doi: 10.1021/jacs.5b11740.
22. C. P. Clark, J. E. Mann, J. S. Bangsund, W.-J. Hsu, E. S. Aydil, R. J. Holmes, *ACS Energy Lett.*, **5**, No. 11, 3443 (2020), doi: 10.1021/acsenergylett.0c01609.
23. J. P. Perdew, K. Burke, M. Ernzerhof, *Phys. Rev. Lett.*, **78**, No. 7, 1396 (1997), doi: 10.1103/PhysRevLett.78.1396.
24. G. Kresse, D. Joubert, *Phys. Rev. B*, **59**, No. 3, 1758 (1999), doi: 10.1103/PhysRevB.59.1758.
25. P. E. Blöchl, *Phys. Rev. B*, **50**, No. 24, 17953 (1994), doi: 10.1103/PhysRevB.50.17953.
26. G. Kresse, J. Furthmüller, *Comput. Mater. Sci.*, **6**, No. 1, 15 (1996), doi: 10.1016/0927-0256(96)00008-0.
27. J. Kubler, K. H. Hock, J. Sticht, A. R. Williams, *J. Phys. F: Met. Phys.*, **18**, No. 3, 469 (1988), doi: 10.1088/0305-4608/18/3/018.
28. U. V. Barth, L. Hedin, *J. Phys. C: Solid State Phys.*, **5**, No. 13, 1629 (1972), doi: 10.1088/0022-3719/5/13/012.
29. A. G. Redfield, *IBM J. Res. Dev.* **1**, No. 1, 19 (1957), doi: 10.1147/rd.11.0019.
30. J. M. Jean, R. A. Friesner, G. R. Fleming, *J. Chem. Phys.*, **96**, No. 8, 5827 (1992), doi: 10.1063/1.462858.
31. A. Einstein, *Phys. Z.*, **18**, 121 (1917).
32. M. Kasha, *Discuss. Faraday Soc.*, **9**, 14 (1950), doi: 10.1039/DF9500900014.
33. Y. Fu, W. Zheng, X. Wang, M. P. Hautzinger, D. Pan, L. Dang, J. C. Wright, A. Pan, S. Jin, *J. Am. Chem. Soc.*, **140**, No. 46, 15675 (2018), doi: 10.1021/jacs.8b07843.